

A universal principle for a rational design of single-atom electrocatalysts

Haoxiang Xu¹, Daojian Cheng^{1,2*}, Dapeng Cao^{1,2*} and Xiao Cheng Zeng^{1,3*}

Developing highly active single-atom catalysts for electrochemical reactions is a key to future renewable energy technology. Here we present a universal design principle to evaluate the activity of graphene-based single-atom catalysts towards the oxygen reduction, oxygen evolution and hydrogen evolution reactions. Our results indicate that the catalytic activity of single-atom catalysts is highly correlated with the local environment of the metal centre, namely its coordination number and electronegativity and the electronegativity of the nearest neighbour atoms, validated by available experimental data. More importantly, we reveal that this design principle can be extended to metal-macrocycle complexes. The principle not only offers a strategy to design highly active nonprecious metal single-atom catalysts with specific active centres, for example, Fe-pyridine/pyrrole-N₄ for the oxygen reduction reaction; Co-pyrrole-N₄ for the oxygen evolution reaction; and Mn-pyrrole-N₄ for the hydrogen evolution reaction to replace precious Pt/Ir/Ru-based catalysts, but also suggests that macrocyclic metal complexes could be used as an alternative to graphene-based single-atom catalysts.

Energy conversion and storage technologies, such as water electrolyzers, metal-air batteries and fuel cells, have attracted extensive interests due to their merits of clean and sustainable ways in producing or consuming molecular hydrogen (H₂), an alternative energy source to fossil fuels¹. In these renewable energy technologies, precious-metal-group (PMG) materials (for example, platinum and noble metal oxides) are commonly utilized as state-of-the-art electrocatalysts^{2,3} for the oxygen reduction reaction (ORR), oxygen evolution reaction (OER) and hydrogen evolution reaction (HER). However, the high cost and scarcity of PMG materials limit their large-scale and sustainable applications⁴. Apart from developing metal-free catalysts⁵, alloying with cheaper elements is one strategy to lower the cost and enhance the performance of PMG catalysts⁶. In addition, PMG materials are generally downsized to provide the highest number of active sites in the catalyst and achieve the maximum utilization efficiency. Single-atom catalysts (SAC), which represent the lowest size for a metal catalyst, have recently emerged as a new research frontier in catalysis^{7,8}.

Recently, so-called M–N–C-based SACs, where M–N–C refers to as the trace metal (M, typically cost-effective transition metals, such as Fe, Co or Ni) and nitrogen (N) co-doped on the graphene support (C), have been widely considered as promising substitutes for PMG electrocatalysts^{9–17}. SAC-like metal-macrocycle complexes have also been reported as excellent molecular electrocatalysts with similar active sites as those in SACs on graphene^{18,19}. A major advantage of the metal-macrocycle molecule combination is that the metal atom is embedded in the same molecular support with an identical local coordination environment, compared with the diverse local coordination environments simultaneously found for a given SAC on graphene. Such SAC-like metal-macrocycle complexes can overcome the tendency toward the formation of crystalline particles and amorphous carbon^{20,21}, which could occur during the synthesis through pyrolysis of M–N–C-based SACs on carbon support^{22,23}. Although graphene-supported SACs have demonstrated

superior electrocatalytic activities, trial-and-error approaches are still a common practice to search for highly efficient catalysts in the laboratory, largely due to the lack of a universal design principle to guide the search. To achieve a rational design of optimal catalysts, it is important to identify the characteristics of the active site. Most recently, several theoretical models have been reported to correlate the catalytic activity of electrocatalysts with some of their properties, such as the adsorption strength of reaction intermediates (H*, OH*, O* and OOH*)^{6,24}, the location of the *d*-band centre for transition-metal alloys²⁵, the valence band for non-metallic carbon materials²⁶, the *e_g* filling for perovskites²⁷, the density of coordinatively unsaturated metal centres for transition-metal oxides²⁸ and the generalized coordination for metallic catalysts²⁹. However, a universal design principle is still lacking to provide a universal description of the relationship between intrinsic properties of the active centre and the catalytic activity of supported SACs.

Here we present a universal design principle that can be used for the rational design of SACs toward highly efficient and cost-effective electrocatalysts, and further reveal that the local structural and chemical environment of the active centres can serve as a universal descriptor to predict the ORR/OER/HER activities for graphene-based SACs. Moreover, the identified descriptor is validated by available experimental data. We also demonstrate that the newly identified universal descriptor can be extended to describe SAC-like metal-macrocycle complexes, and that both types of SAC can give rise to the same activity trends.

Results

Calculated electrocatalytic activity. Many previous experimental studies and theoretical simulations have shown that the realistic active sites of SACs supported on graphene are actually isolated metal atoms coordinated by pyridine/pyrrole nitrogen atoms, carbon atoms or hybrid of C and N (refs ^{20,30–32}). Based on these previous studies, we constructed a total of 112 SACs models, in which

¹Beijing Advanced Innovation Center for Soft Matter Science and Engineering, Beijing University of Chemical Technology, Beijing, China. ²State Key Laboratory of Organic-Inorganic Composites, Beijing Key Laboratory of Energy Environmental Catalysis, Beijing University of Chemical Technology, Beijing, China. ³Department of Chemistry, Department of Chemical & Biomolecular Engineering, and Department of Mechanical & Materials Engineering, University of Nebraska, Lincoln, NE, USA. *e-mail: chengdj@mail.buct.edu.cn; caodp@mail.buct.edu.cn; xzeng1@unl.edu

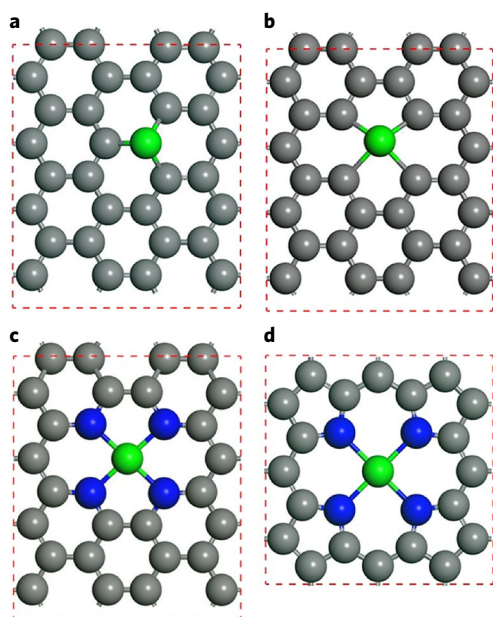


Fig. 1 | Schematic of a single TM atom supported on graphene with different coordination environments. **a**, Single vacancy with three carbon atoms (SV-C₃). **b**, Double vacancy with four carbon atoms (DV-C₄). **c**, Four pyridine nitrogen atoms (pyridine-N₄). **d**, Four pyrrole nitrogen atoms (pyrrole-N₄). The green, blue and grey colours represent TM, N and C atoms, respectively. The unit cells are marked in red.

3d, 4d and 5d single transition-metal (TM) atoms are doped in a graphene sheet with different coordination environments, including (1) a single vacancy with three carbon neighbours (SV-C₃, Fig. 1a), (2) a double vacancy with four carbon neighbours (DV-C₄, Fig. 1b), (3) four pyridine nitrogen atoms (pyridine-N₄, Fig. 1c) and (4) four pyrrole nitrogen atoms (pyrrole-N₄, Fig. 1d).

According to the typical experimental electrocatalytic conditions for SACs supported on graphene, we first evaluated ORR and OER performance in an alkaline electrolyte and HER performance in an acidic electrolyte (computational details and results are given in Methods and Supplementary Tables 1–6). The free-energy diagram for the ideal ORR or OER catalyst is shown in Supplementary Fig. 1a,b. To facilitate O₂ reduction at the equilibrium potential, the reaction free energies of all four proton-transfer steps should be the same (4.92 V/4 = 1.23 V versus reversible hydrogen electrode (RHE)) at zero potential for an ideal catalyst. In other words, all reaction free energies should be zero when the onset potential equals the equilibrium potential, 1.23 V. As shown in Supplementary Fig. 2, the overall HER mechanism is evaluated by a three-state diagram consisting of an initial H⁺ state, an intermediate H* state and 1/2H₂ as the final product. The ideal catalyst for HER has zero ΔG_{H^*} to achieve zero overpotential η , since the adsorbed H can be as stable as solvated proton and gas-phase hydrogen at zero potential (equilibrium potential).

The computed free-energy diagrams for the ORR on the Pt(111) surface (a widely used theoretical model for commercial Pt/C) are shown in Supplementary Table 7 and Supplementary Fig. 1c. All elementary steps proceed spontaneously at zero potential relative to the RHE ($U_{\text{RHE}} = 0$ V) from the viewpoint of thermodynamics, since all electron transfer steps are exergonic ($\Delta G < 0$). When the output potential increases to $U_{\text{RHE}} = 0.80$ V, the free energy of the last electron-transfer step becomes zero while the other steps remain downhill, indicating that ORR cannot proceed spontaneously for $U_{\text{RHE}} > 0.80$ V because the last step becomes endergonic ($\Delta G > 0$). Hence, $U_{\text{RHE}} = 0.80$ V is the onset potential

($U_{\text{RHE}}^{\text{onset}}$) for the ORR on Pt(111) (Supplementary Table 8). The free-energy diagrams of OER on IrO₂(110) (the common theoretical model for commercial IrO₂) are shown in Supplementary Table 7 and Supplementary Fig. 1d. It can be seen that at $U_{\text{RHE}} = 0$ V all the elementary steps are uphill. OER can only proceed spontaneously as the potential increases above the onset potential (for $U_{\text{RHE}} > 1.88$ V), because all electron-transfer steps are exergonic ($\Delta G < 0$). Therefore, $U_{\text{RHE}} = 1.88$ V is the onset potential ($U_{\text{RHE}}^{\text{onset}}$) for the OER on IrO₂(110) (Supplementary Table 8).

According to a previous definition³³, the lower the absolute deviation between $U_{\text{RHE}}^{\text{onset}}$ and equilibrium potential (U_{RHE}^0 , 1.23 V), the higher the ORR and OER electrocatalytic performance. As shown in Supplementary Fig. 2, a more desirable catalyst than Pt(111) would have free energy for H adsorption (ΔG_{H^*}) closer to zero to compromise the reaction barriers of the hydrogen adsorption and desorption steps to achieve less overpotential (η) for HER than Pt(111) (Supplementary Table 8). We calculated the reaction free energy for each elementary step (Supplementary Tables 9–12) of ORR and OER. Supplementary Figs. 3–14 show the free-energy diagrams of ORR, OER and HER on all SAC models at zero potential, from which the $U_{\text{RHE}}^{\text{onset}}$ for ORR and OER and the η for HER can be calculated. The results are listed in Supplementary Tables 13–16. Apart from electrocatalytic performance, we also examined the stability of the SACs against either metal atom aggregation or metal being leached, on a theoretical level, to confirm that the predicted catalysts are experimentally feasible (computational details and results are given in Methods and Supplementary Table 17, respectively).

Adsorption–activity relationships. Insights into distinct ORR, OER and HER performance with different SACs can guide the design of better electrocatalysts. As shown in Supplementary Methods, the reaction free energy of each elementary step is determined by the adsorption free energies of the reaction intermediates OH*, O*, OOH* and H*. In other words, the diverse ORR, OER and HER performance stems from different binding strengths of the adsorption species on different catalysts. Therefore, it is crucial to identify the relationship between the adsorption free energies of reaction intermediates and catalytic activity for rational search of more-effective catalysts. In Fig. 2a, the calculated adsorption free energy for OOH* and O* (ΔG_{OOH^*} and ΔG_{O^*}) is plotted versus that for OH* (ΔG_{OH^*}) on all SACs. The following linear relationships can be fitted from the data points through linear regression:

$$\Delta G_{\text{OOH}^*} = 0.92 \times \Delta G_{\text{OH}^*} + 3.14 \quad (1)$$

$$\Delta G_{\text{O}^*} = 1.87 \times \Delta G_{\text{OH}^*} + 0.22 \text{ (for } \Delta G_{\text{OH}^*} > -0.7 \text{ eV)} \quad (2)$$

$$\Delta G_{\text{O}^*} = -1.59 \times \Delta G_{\text{OH}^*} - 2.30 \text{ (for } \Delta G_{\text{OH}^*} < -0.7 \text{ eV)} \quad (3)$$

The data points of ΔG_{OOH^*} versus ΔG_{OH^*} can be nicely correlated by the fitted line whose slope and intercept are very similar to those measured with the metal-based material surfaces^{34,35}. The data points of ΔG_{O^*} versus ΔG_{OH^*} exhibit a piecewise relationship. For metal elements from the VIB group to the IIB group ($\Delta G_{\text{OH}^*} > -0.7$ eV), the linear section has similar slope and intercept as those reported in previous theoretical works^{34,35}, while the other linear section ($\Delta G_{\text{OH}^*} < -0.7$ eV) displays different relation between ΔG_{O^*} and ΔG_{OH^*} for metal atoms from group IIIB to group VB. Such a piecewise relationship has also been seen for O₂ adsorption on metal-doped graphene³⁶. According to the relationships between ΔG_{OOH^*} , ΔG_{O^*} and ΔG_{OH^*} given above, ΔG_{OH^*} can be considered as the only independent variable to describe the $U_{\text{RHE}}^{\text{onset}}$ for ORR and OER in all SAC systems. According to the relationship between η^{HER} and ΔG_{H^*} shown in Supplementary Fig. 2, the overpotentials of HER can be described only by ΔG_{H^*} .

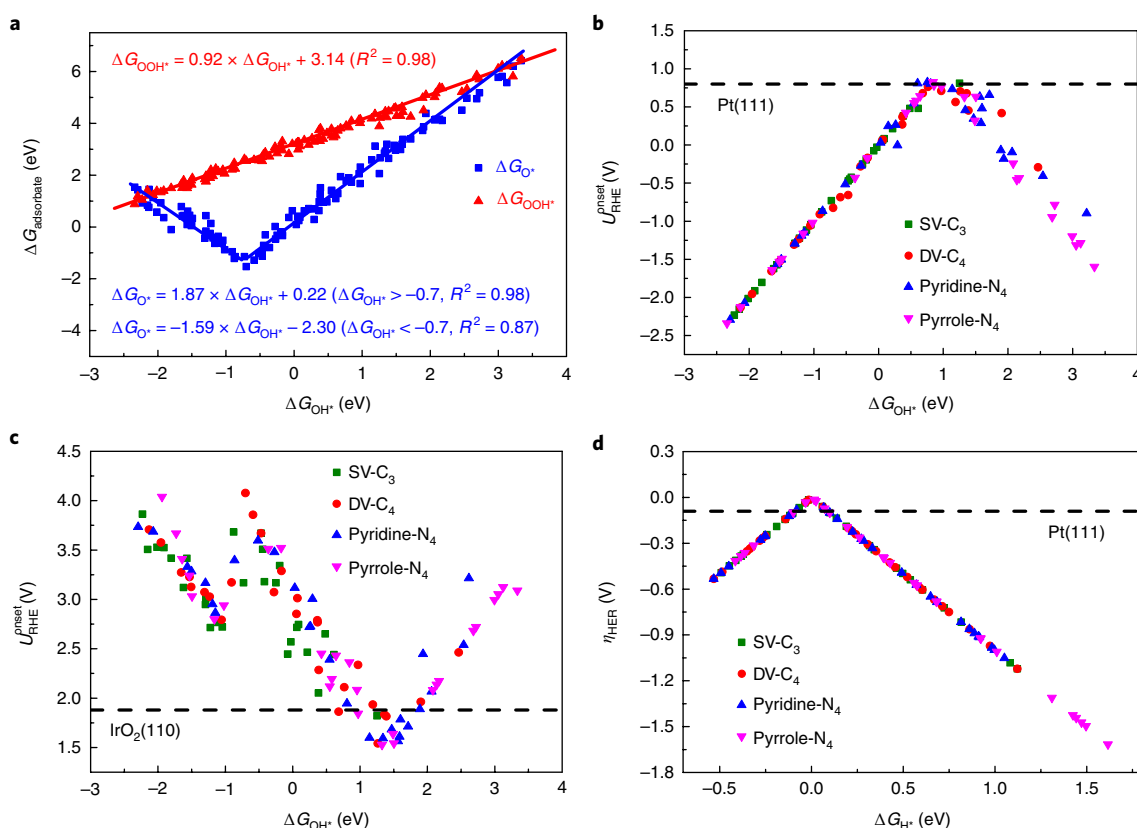


Fig. 2 | Adsorption free energies of adsorbates and electrocatalytic activity as a function of ΔG_{OH^*} and ΔG_{H^*} . **a**, Adsorption free energies of OOH and O versus that of OH on all single TM atoms supported on graphene. **b**, ORR theoretical onset potential versus adsorption free energies ΔG_{OH^*} on all single TM atoms supported on graphene. **c**, OER theoretical onset potential versus adsorption free energies ΔG_{OH^*} on all single TM atoms supported on graphene. **d**, HER theoretical overpotential versus adsorption free energies ΔG_{H^*} on all single TM atoms supported on graphene. The theoretical onset potential of Pt(111) for ORR and IrO₂(110) for OER and overpotential of Pt(111) for HER are also plotted in **b–d**.

With the established activity indicators (ΔG_{OH^*} and ΔG_{H^*}) for ORR, OER and HER, the plotted theoretical U_{onset} versus ΔG_{OH^*} , and η_{HER} versus ΔG_{H^*} for all single TM atoms supported on graphene exhibit universal volcano relationships (see Fig. 2b–d). As shown in Supplementary Tables 9–12, the potential-determining step in ORR can either be protonation of O₂ to OOH* or the desorption of OH* to OH[−]. Based on the expression of $\Delta G_1/\Delta G_4$ (equations (24) and (27)) containing ΔG_{OOH^*} and ΔG_{OH^*} , and the linear relation between ΔG_{OOH^*} and ΔG_{OH^*} , both legs of the volcano shown in Fig. 2b are linear. In OER, the potential-determining steps can be either the formation of O* from OH* or the transformation of O* to OOH*. Based on the expression of $\Delta G_6/\Delta G_7$ (equations (30) and (31)) consisting of ΔG_{OOH^*} , ΔG_{O^*} and ΔG_{OH^*} , and the piecewise relationship between ΔG_{O^*} and ΔG_{OH^*} , one of the legs of volcano is piecewise linear in Fig. 2c. Combined with Fig. 2b,c, when ΔG_{OH^*} is less than 1 eV, both U_{onset} for the ORR and OER are in the left branch of the volcano plot, indicating that the performance of both reactions is enhanced with weaker OH* adsorption. In contrast, when ΔG_{OH^*} is greater than 1.5 eV, both U_{onset} for the ORR and OER are in the right branch of the volcano plot, indicating better performance with stronger OH* adsorption. In the zone between 1 and 1.5 eV, U_{onset} for ORR and U_{onset} for OER decrease or increase simultaneously. Hence, in this zone, SACs with both optimal ORR and OER cannot be met, suggesting that a performance ceiling exists for single TM atoms supported on graphene (serving as bifunctional oxygen electrodes). Nevertheless, it is worth mentioning that for a material with appropriate OH* adsorption strength within 1–1.5 eV, such as Co-pyridine-N₄, it would still give outstanding bifunctional

performance for ORR and OER. In Fig. 2d, the volcano relationship between η_{HER} and ΔG_{H^*} agrees with previous theoretical works in which ΔG_{H^*} can be considered as a useful descriptor for HER catalytic activity³⁷. Either H binding to the surface that is too weak (H⁺ cannot be captured from the dissolved phase) or H binding that is too strong (gaseous H₂ will have difficulty to leave the surface) would restrain the HER activity (η_{HER} being away from zero).

Universal descriptor. Although the adsorption free energies of intermediates (ΔG_{OH^*} and ΔG_{H^*}) exhibit correlation with the ORR, OER and HER activity, the intrinsic characteristics of the active centre that dominates the adsorbate binding strength is uncertain. In fact, it is impractical to directly engineer the catalytic centre to tune ΔG_{OH^*} or ΔG_{H^*} towards the optimal values through the adsorption–activity relationship. Also, tailoring the adsorption energy of intermediates to achieve desirable activity is highly unrealistic in experiments, due to the challenge in directly measuring the adsorption properties of the intermediates in the electrocatalysis condition³⁸. Thus, the descriptors of ΔG_{OH^*} and ΔG_{H^*} are inconvenient for the purpose of fast-scan/estimation, and they lack the predictive power to guide the rational design of new catalysts. Therefore, it is important to identify intrinsic properties of the catalytic centre, which are readily accessible in the laboratory, to adjust the adsorption energy of intermediates and activity.

Here, we focus on the valence electrons in the occupied *d* orbital of the metal element (θ_d) derived from the periodic table. We first plot ΔG_{OH^*} and ΔG_{H^*} versus θ_d , respectively, by considering the fact that electrons in the occupied *d* orbital of metal have been proven

as a significant factor for the adsorption strength³⁹. However, as seen in Supplementary Fig. 15a,b, widespread data points in ΔG_{OH^*} and ΔG_{H^*} are observed at the same value of θ_d . This spread indicates that θ_d alone cannot correlate ΔG_{OH^*} and ΔG_{H^*} well for SACs. To consider the redistribution of θ_d stemming from the interaction between metal atom and adsorbate, we add an additional factor to θ_d by introducing electronegativity (Supplementary Table 18). It is known that the electronegativity quantifies the electron affinity of certain elements when the corresponding covalent bond is formed. The difference in electronegativity between the metal atom and attachment atom of adsorbate (O atom for OH^* and H atom for H^*) may be strongly related to the redistribution of θ_d . Thus, we plot ΔG_{OH^*} and ΔG_{H^*} versus $\theta_d \times E_{\text{M}}/E_{\text{O}}$ and $\theta_d \times E_{\text{M}}/E_{\text{H}}$ in Supplementary Fig. 15c,d (E_{M} , E_{O} and E_{H} represent the electronegativity of metal element, oxygen element and hydrogen element, respectively). The plots show that the modified descriptor can correlate with ΔG_{OH^*} and ΔG_{H^*} better for SACs in the same coordination environment. The widespread of ΔG_{OH^*} and ΔG_{H^*} among SACs in different coordination environments implies that local environment of the active centre may impact catalytic reactivity. Actually, this assumption can be testified to a certain extent by some experimental observations in combination with DFT calculations. For example, controllable synthesis of single cobalt atoms can reach superior electrochemical activity by tuning C/N hybrid coordination precisely, because C/N hybrid coordination can enhance the electron transfer, which promotes the adsorption and reaction kinetics of the intermediates^{40,41}. So we consider the single TM atom together with its nearest neighbours as the active centre and further modify the descriptor as following:

$$\varphi = \theta_d \times \frac{E_{\text{M}} + \alpha \times (n_{\text{N}} \times E_{\text{N}} + n_{\text{C}} \times E_{\text{C}})}{E_{\text{O/H}}} \quad (4)$$

where E_{N} and E_{C} represent the electronegativity of nitrogen and carbon elements, n_{N} and n_{C} represent the number of nearest-neighbour N and C atoms, and α is the correction coefficient. We compared the nearest-neighbour atoms in single-TM-atom-pyrrole- N_4 with those in other catalytic centres (Fig. 1), pyrrole nitrogen atoms combine with four carbon atoms to form a ring while the nearest-neighbour atoms in other catalytic centres combine with five carbon atoms, which enhances the ability of single-TM-atom-pyrrole- N_4 to accept electrons due to a smaller electron source in the graphene sheet. Thus, α is set to $5/4 = 1.25$ for single-TM-atom-pyrrole- N_4 while $\alpha = 1$ for the other catalytic centres.

Valence electrons in the d orbital (θ_d), electronegativity and the corresponding descriptor, φ , of a single-TM-atom with different coordination environments are listed in Supplementary Tables 19–22. It is found that the descriptor φ can exhibit a linear relationship when plotted against adsorption energies of ΔG_{OH^*} and ΔG_{H^*} in Fig. 3a,b. The following linear relationships can be fitted from the data set through linear regression:

$$\Delta G_{\text{OH}^*} = 0.11 \times \varphi - 2.48 \quad (5)$$

$$\Delta G_{\text{H}^*} = -0.07 \times \varphi + 1.27 \quad (\varphi < 27) \quad (6)$$

$$\Delta G_{\text{H}^*} = 0.04 \times \varphi - 1.43 \quad (\varphi > 27) \quad (7)$$

The relationship between φ and ΔG_{OH^*} indicates that an increase in φ corresponds to a decrease in binding strength, and this can be attributed to the electronic structure of active centre binding with adsorbate. According to the expression of φ , the higher value of φ means that the single-TM-atom possesses more valence

electrons of the d orbital after charge redistribution. As shown in Supplementary Fig. 16, SACs with higher work function (need more energy to remove an electron) possess more valence electrons in the metal atom (larger φ). This result validates our descriptor φ . Based on the previously reported d -band centre model³⁹, the relationship between the adsorption strength of a metal atom and its d -band electronic structure can be demonstrated by the scheme for bond formation as illustrated in Supplementary Fig. 17. Namely, the electronic states of the metal atom interact with that of hydroxyl when forming OH^* on the metal atom. Consequently, their hybridized energy levels split into two groups. One is the bonding states that are generally occupied under the Fermi Level, and the other is the anti-bonding orbital that lies above the Fermi level. A change in the adsorption strength is due to the anti-bonding states, that is, a lower d -band centre location (more electrons in the d orbital) of the active sites makes the anti-bonding states with lower level and higher occupancy, leading to the weaker interaction between the adsorbate and catalyst surface, and vice versa. Accordingly, we also introduce the band centre of the anti-bonding orbital ($E_{\text{anti-bond}}$, equation (36)) for the binding between single-TM-atom and OH^* by calculating the projected density of states (pDOS) for the d orbital of a single-TM-atom and p orbital of a O atom belonging to OH^* (see Supplementary Figs. 18–21). As shown in Supplementary Fig. 22, a clear shift of $E_{\text{anti-bond}}$ to low energy level and weakened binding strength of OH^* are seen with the increase of φ , consistent with the bond formation analysis above.

As for the relationship between φ and ΔG_{H^*} , it shows the same trend as that between φ and ΔG_{OH^*} for $\varphi > 27$. However, for $\varphi < 27$, ΔG_{H^*} becomes a decreasing function of φ , demonstrating that with increasing the d -band energy level (less electrons in the d orbital), the H^* adsorption strength decreases, contrary to the observed trend for $\varphi > 27$. This difference can be explained by the fact that when the value of φ is too low, the bonding orbital for the binding between single-TM-atom and H^* is mainly distributed near the Fermi level rather than located at a deeper level⁴². With an upward shifting of d orbitals (less electrons in the d orbital), the bonding orbital upshifts as well, leading to a decreasing occupancy (receded H^* adsorption strength).

Using the simple descriptor φ for which all parameters are intrinsic properties of the active centre, we can use it to replace ΔG_{OH^*} and ΔG_{H^*} , and derive a volcano relationship for U_{onset} of ORR/OER and η_{HER} versus φ in Supplementary Fig. 23. Here, Pt(111) and $\text{IrO}_2(110)$ were considered as the benchmark systems (as commercial Pt/C and IrO_2 are usually regarded as the reference electrocatalysts in experiments) to search for optimal SACs supported on graphene in order to achieve better electrocatalysis performance than Pt(111) or $\text{IrO}_2(110)$. As shown in Supplementary Fig. 23a, among all single TM atoms supported on graphene, only catalysts with φ values in the range 30–32 show the higher U_{onset} for ORR than that of Pt(111). It is noted that Fe-pyridine- N_4 , Co-pyridine- N_4 and Fe-pyrrole- N_4 are predicted to be the best catalysts, as demonstrated by many previous experiments^{13,31,43}. Some other promising candidates, such as Pt-DV- C_4 , Tc-pyrrole- N_4 and Os-pyrrole- N_4 , also possess comparable ORR catalytic activities to previously reported SACs, and the predicted SACs with sufficient stability in theory (Supplementary Table 17) can be readily tested by future experiments. As shown in Supplementary Fig. 23b, the superior SACs over $\text{IrO}_2(110)$ for OER are predicted to have φ values in the range 30–35. Previous experiments have shown that the electrocatalysts with Co-pyridine- N_4 and Ni-pyridine- N_4 active centre give better catalytic performance than the commercial IrO_2 (refs^{44,45}), and the results of experiments are fully consistent with our prediction. In addition, we identified several other active centres with outstanding OER activity, such as Ni/Cu/Zn-DV- C_4 , Cu/Ru/Rh/Ir-pyridine- N_4 and Co/Ru/Ir-pyrrole- N_4 , which satisfy the stability criterion (Supplementary Table 17). It is expected that these catalysts can be synthesized experimentally.

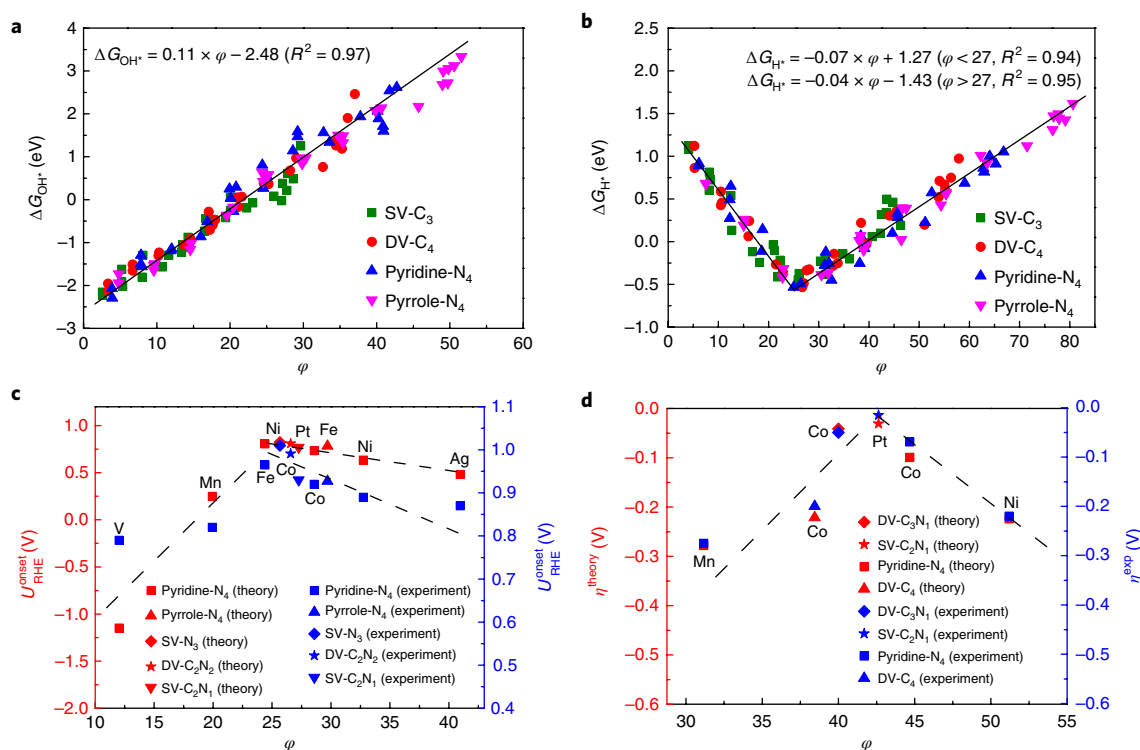


Fig. 3 | ΔG_{OH^*} , ΔG_{H^*} and electrocatalytic activity as a function of descriptor ϕ . **a**, Adsorption free energy of OH versus the descriptor ϕ for all single TM atoms supported on graphene. **b**, Adsorption free energy of H versus the descriptor ϕ for all single TM atoms supported on graphene. **c**, Theoretical and corresponding experimental onset potentials for ORR versus the descriptor ϕ . **d**, Theoretical and corresponding experimental overpotentials for HER versus the descriptor ϕ . The dashed lines represent the general relationship between the activity of ORR/HER and the descriptor ϕ .

Although these active centres have outstanding catalytic activity for OER, graphene-supported catalysts may suffer from extremely limited lifetimes due to electrochemical corrosion of the carbon support under the high electrochemical oxidizing potentials of OER catalysis, which should be noticed in future experiments. As shown in Supplementary Fig. 23c, an optimal catalyst with ϕ around 17 or 39 can balance the reaction barriers of the H^+ reduction and H_2 desorption to achieve zero overpotential η . Other candidates with catalytic activities comparable to Pt(111) for HER ($\eta = 0.09$ V) include: (1) Co-pyridine- N_4 , which has been synthesized experimentally⁴⁶, and (2) Cr/Mn/Zn/Pt-SV- C_3 , Ru/Ta/Ir-DV- C_4 and Mn/Fe/Mo/Re-pyrrole- N_4 , which favour to be embedded into the graphene rather than aggregation (Supplementary Table 17). These theoretical predictions need future experimental confirmation. We also examine whether solvation could change the promising SACs that we identified using the descriptor ϕ . The corresponding adsorption free energies of adsorbates, reaction energy of each elementary steps, as well as electrocatalytic activity on SACs with solvation corrections are listed in Supplementary Tables 23 and 24. As shown in Supplementary Table 24, the identified promising SACs marked with red in Supplementary Tables 13–16 still possess not only higher $U_{\text{ORR}}^{\text{onset}}$ than Pt(111), but also lower $U_{\text{OER}}^{\text{onset}}$ than IrO_2 (110), indicating that solvation effects seem to have little influence on the application of the universal design principle for identifying promising electrocatalyst candidates presented in this work.

To verify the volcano relationship between ϕ and the activity, we construct the relationships between ϕ and catalytic activity measured in linear scan voltammogram (LSV) experiments. We summarize in Supplementary Table 25 the experimental $U_{\text{ORR}}^{\text{onset}}$ and η^{HER} reported for single TM atoms supported on graphene. The theoretical results of corresponding single TM atoms with C/N hybrid coordination are listed in Supplementary Table 26. Figure 3c shows the experimental $U_{\text{ORR}}^{\text{onset}}$ (blue dots) and theoretical $U_{\text{ORR}}^{\text{onset}}$ (red dots) of single TM atoms

supported on graphene versus the descriptor ϕ . As indicated by the dashed line, the relative order of catalytic activity from experiment is consistent with the theoretical prediction. The same volcano relationships between the η^{HER} and ϕ for experimental/theoretical results are also shown in Fig. 3d. Notably, the consistency between experimental data and theoretical predictions supports that the descriptor ϕ is highly correlated with the HER activity of single TM atoms supported on graphene. To exclude the measurement deviation from different experiment works, we also compare the ORR theoretical activity with the catalytic activity measured in the same experiment, as shown in Supplementary Fig. 24. We can still reproduce the order of the activity reported in the available experiments. Hence, ϕ is shown as a universal descriptor for the ORR, OER and HER activity of single TM atoms supported on graphene materials.

Extension to macrocyclic molecules. The identified descriptor ϕ suggests that the intrinsic properties of the local environment of the catalytic centre play a key role in the activity of SACs on graphene. To further confirm the rationality that ϕ can describe intrinsic effects of the local environment of the active centre on adsorbate properties and activity, we also investigated ORR, OER and HER performance on single TM atoms coordinated with macrocyclic molecules (Fig. 4a–d) with the same coordination environment as those on graphene (Fig. 1). As shown in Supplementary Tables 27–30 and Fig. 4e,f, the scaling relations that correlate $\Delta G_{\text{OH}^*}/\Delta G_{\text{H}^*}$ with ϕ , established above for single TM atoms supported on graphene, are equally suitable for single TM atoms coordinated with macrocyclic molecules. In addition to the prediction of adsorption energies of intermediates based on descriptor ϕ , Tables 1–3 show that $U_{\text{ORR}}^{\text{onset}}$, $U_{\text{OER}}^{\text{onset}}$ and η^{HER} derived from the free-energy diagrams of ORR, OER and HER (Supplementary Tables 31 and 32 and Supplementary Figs. 25–27) for single TM atoms coordinated with macrocyclic molecules have an acceptable absolute difference

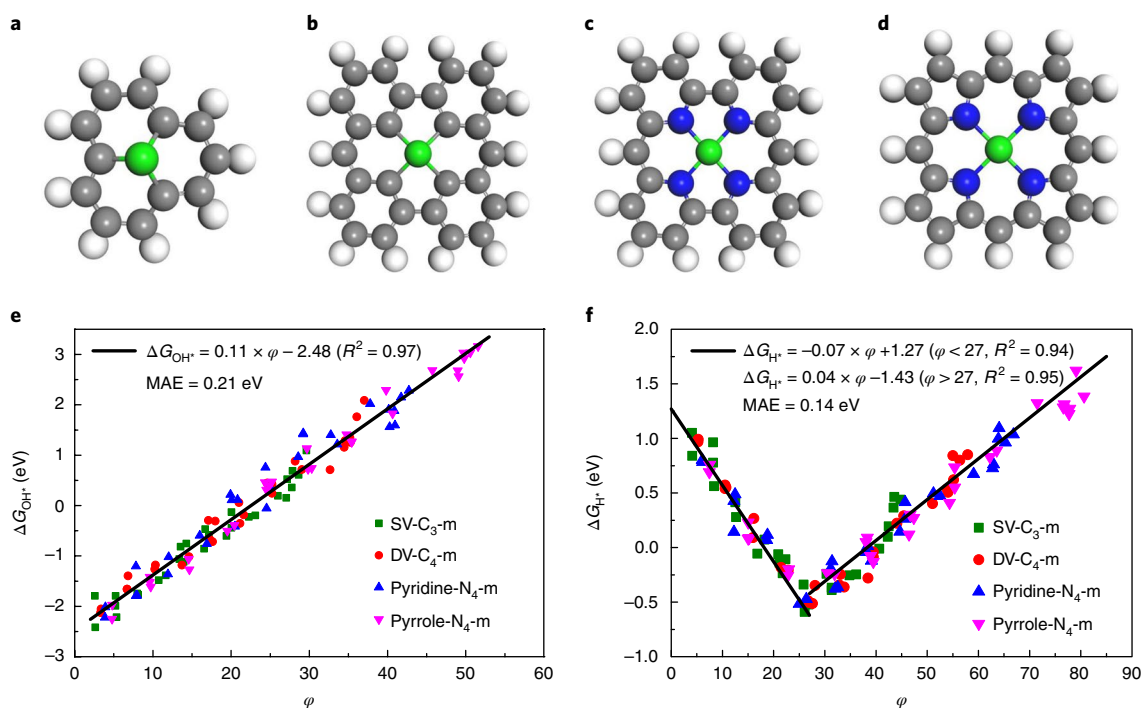


Fig. 4 | Extension of descriptor ϕ to SAC-like metal-macrocycle complexes. **a–d**, Schematic of SAC-like metal-macrocycle complexes with different coordination environments, single vacancy with three carbon atoms (SV-C₃-m) (**a**), double vacancy with four carbon atoms (DV-C₄-m) (**b**), four pyridine nitrogen atoms (pyridine-N₄-m) (**c**) and four pyrrole nitrogen atoms (pyrrole-N₄-m) (**d**). **e**, Scatter of adsorption free energy of OH versus the descriptor ϕ for all single TM atoms supported on macrocyclic molecules. **f**, Scatter of adsorption free energy of H versus the descriptor ϕ for all single TM atoms supported on macrocyclic molecules. The black line represents the function in Fig. 3a,b. Mean absolute differences (MAE) between predicted values based on the black line and calculated values are also given.

Table 1 | A list of theoretical onset potentials (eV) for ORR on single TM atoms supported on graphene and macrocyclic molecules, and the absolute difference between them.

Active centre	Macrocyclic molecule	Graphene	Absolute difference
Au-SV-C ₃	0.79	0.81	0.02
Pt-DV-C ₄	0.70	0.76	0.06
V-pyridine-N ₄	−1.02	−1.15	0.13
Mn-pyridine-N ₄	0.22	0.25	0.03
Fe-pyridine-N ₄	0.76	0.81	0.05
Co-pyridine-N ₄	0.83	0.73	0.10
Ni-pyridine-N ₄	0.67	0.63	0.04
Ag-pyridine-N ₄	0.55	0.48	0.07
Fe-pyrrole-N ₄	0.71	0.78	0.07
Tc-pyrrole-N ₄	0.72	0.83	0.11
Os-pyrrole-N ₄	0.74	0.76	0.02

(less than 0.2 eV) compared with those for single TM atoms supported on graphene, indicating again the applicability of the universal descriptor ϕ for single TM atoms coordinated with macrocyclic molecules. All these results confirm that the local environment of the active sites, including the isolated metal atom, its nearest neighbours and coordination number, is indeed the intrinsic characteristic that dictates the catalytic performance. Note that similar active sites have been observed in many macrocyclic molecular systems or biomolecules (for example, metal porphyrins, metallophthalocyanine and enzymes) which also exhibit superior catalytic activity for electrochemical reactions^{18,19,47}.

Table 2 | A list of theoretical onset potentials (eV) for OER on single TM atoms supported on graphene and macrocyclic molecules, and the absolute difference between them.

Active centre	Macrocyclic molecule	Graphene	Absolute difference
Au-SV-C ₃	1.97	1.82	0.15
Ni-DV-C ₄	1.98	1.86	0.12
Cu-DV-C ₄	1.88	1.83	0.05
Zn-DV-C ₄	1.58	1.54	0.04
Cd-DV-C ₄	1.77	1.81	0.04
Co-pyridine-N ₄	1.73	1.60	0.13
Ni-pyridine-N ₄	1.52	1.56	0.04
Cu-pyridine-N ₄	1.88	1.71	0.17
Ru-pyridine-N ₄	1.83	1.68	0.15
Rh-pyridine-N ₄	1.70	1.59	0.11
Ag-pyridine-N ₄	1.87	1.78	0.09
Cr-pyridine-N ₄	1.72	1.89	0.17
Ir-pyridine-N ₄	1.57	1.61	0.04
Co-pyrrole-N ₄	1.62	1.54	0.08
Ru-pyrrole-N ₄	1.63	1.64	0.01
Ir-pyrrole-N ₄	1.55	1.53	0.02

Discussion

The newly identified universal descriptor ϕ exhibits an intrinsic relationship with intermediate adsorption, and thus with catalytic activities. Compared with state-of-the-art descriptors such as orbital-

Table 3 | A list of theoretical overpotentials (eV) for HER on single TM atoms supported on graphene and macrocyclic molecules, and the absolute difference between them.

Active centre	Macrocyclic molecule	Graphene	Absolute difference
Cr-SV-C ₃	−0.14	−0.10	0.04
Mn-SV-C ₃	−0.06	−0.04	0.02
Zn-SV-C ₃	0.10	0.10	0.00
Pt-SV-C ₃	−0.01	0.06	0.07
Ru-DV-C ₄	−0.04	−0.02	0.02
Ta-DV-C ₄	0.09	0.06	0.03
Ir-DV-C ₄	−0.09	−0.03	0.06
Co-pyridine-N ₄	0.14	0.10	0.04
Tc-pyridine-N ₄	0.01	0.07	0.06
Cr-pyrrole-N ₄	0.09	0.07	0.02
Mn-pyrrole-N ₄	0.05	0.01	0.04
Fe-pyrrole-N ₄	0.12	0.02	0.10
Mo-pyrrole-N ₄	−0.13	−0.03	0.10
Re-pyrrole-N ₄	−0.08	−0.10	0.02

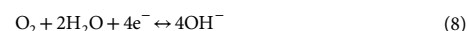
energy theory²⁶ and the work function⁴⁸, ϕ is more directly relevant to material properties and can be conveniently used to predict the catalytic activity of SACs. This is because all parameters associated with ϕ , including the coordination number, the electronegativity of metal atom and its coordination atom, are intrinsic properties of the active centre. Based on the universal design principle, we can reproduce the order of the activity of previously reported experimental SACs on graphene. Moreover, the universal design principle based on the descriptor ϕ can be used to search for the optimal active centre of SACs, for example, Fe-pyridine/pyrrole-N₄ for ORR, Co-pyrrole-N₄ for OER and Mn-pyrrole-N₄ for HER, and to guide experiments to synthesize SACs with the desired active centre that can outperform precious-metal-based commercial catalysts (such as Pt/C and IrO₂). More importantly, the universal design principle can offer a correlation between catalytic activity and electronic structure of the local environment of active sites for SACs supported on both graphene and macrocyclic molecules, suggesting that macrocyclic molecules can be used to replace the graphene as a more uniform and structurally precise support for SACs. Indeed, according to the configuration of an identified superior active site, SACs can be synthesized in the same way as the self-supporting M–N–C molecular catalyst^{20,21} or TM macrocyclic systems^{49,50}, by which more precise atomic structures and higher uniformity local coordination environments for the active centre of SACs can be achieved.

Methods

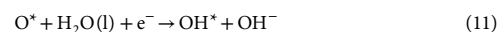
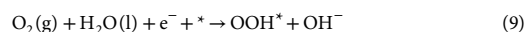
Computational methods and models. The structural optimizations were performed by using first-principle calculations within the framework of density functional theory (DFT), as implemented in the plane wave set Vienna ab initio Simulation Package (VASP) code^{51,52}. The exchange correlation energy was modelled by using Perdew–Burke–Ernzerhof (PBE) functional⁵³ within the generalized gradient approximation (GGA). The projector augmented wave (PAW) pseudo-potentials⁵⁴ were used to describe ionic cores. The cutoff energy of 500 eV was adopted after a series of tests. A Gaussian smearing of 0.05 eV to the orbital occupation is applied during the geometry optimization and for the total energy computations, whilst a tetrahedron method with Blöchl corrections was employed for the accurate electronic structure calculations. It is generally recognized that the localized 3d electrons correlation for transition metal in fourth period can be described by considering on-site coulomb (U) and exchange (J) interactions, a key element in the DFT + U method. Here we applied DFT + U through the rotationally invariant approach⁵⁵ with the corresponding U – J values for different transitions listed in Supplementary Table 33. The convergence threshold for the iteration in self-consistent field (SCF) was set at 10^{−4} eV, and that for geometry optimizations by BFGS algorithm was set to be 0.02 eV Å^{−1}

on maximum force component. The k -point sampling of the Brillouin zone was obtained using a 6 × 7 × 1 grid for the repetitive unit in Fig. 1a–c and 6 × 6 × 1 grid for the repetitive unit in Fig. 1d by Monkhorst–Pack scheme. Denser k -points (12 × 14 × 1 and 12 × 12 × 1) were used for the electronic structure calculations. A large vacuum slab of 15 Å was inserted in the z direction for surface isolation to prevent interaction between two neighbouring surfaces. For commercial Pt/C and IrO₂, we use a p(2 × 2) unit cell of Pt(111) and p(2 × 1) unit cell of IrO₂(110) surface models. The Pt(111) slab has five atom layers and IrO₂(110) has nine atom layers with symmetric terminals. Geometry optimizations for Pt(111) and IrO₂(110) were performed by using the BFGS algorithm with a 5 × 5 × 1 and 5 × 9 × 1 k -mesh, respectively. Top two layers are fully relaxed during structural optimizations while other layers are fixed at the tested lattice positions. Spin polarization was considered in all calculations, and the spin state of each converged configuration is listed in Supplementary Tables 34–37. The vibrational frequencies of free molecules and adsorbates, which are needed to determine zero-point energies and vibrational entropies, were calculated by using the phonon modules in the VASP 5.3 code. We calculate thermodynamic corrections due to solvent effect (G_{sol}) by using VASPsol⁵⁶, which are shown in Supplementary Table 38. Because OH* and OOH* can form H-bonds with H₂O, their adsorption free energies decrease by 0.30 eV, indicating that they are more stable when solvated, consistent with previous theoretical works⁵⁷.

Reaction mechanism. The ORR, OER and HER pathways on SAC systems were calculated in detail according to electrochemical framework developed by Nørskov and his co-workers⁵⁸. As for ORR, in an alkaline electrolyte (pH = 14), H₂O rather than H₃O⁺ may act as the proton donor, so overall reaction scheme of the ORR can be written as:

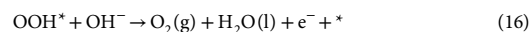
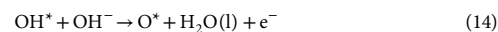


The ORR may proceed through the following elementary steps, which are usually employed to investigate the electrocatalysis of the ORR on various materials:

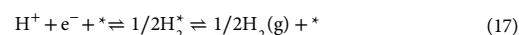


where * stands for an active site on the catalytic surface, (l) and (g) refer to liquid and gas phases, respectively.

The OER occurring in an alkaline electrolyte (pH = 14) through elementary steps takes the reverse direction of ORR:



As for HER, in an acid electrolyte (pH = 0), H⁺ can act as the proton donor, so the overall reaction scheme of the HER can be written as:



where the * represents the adsorption site.

Reaction free energy calculation. For proton-transfer steps, reaction free energies are regarded as approximate values of the activation barriers, because detailed calculations for the transfer of a solvated proton to adsorbed OH[−] show the neglect of overbarriers has been proven as a very good approximation for a situation where the proton transfer is downhill in energy⁵⁹. This approximation may result in a slight overestimation of activity for a given proton-transfer elementary step, but can still qualitatively represent the right relative energetic ordering of the various proton-transfer elementary steps. Therefore, we took the reactions in equations (9)–(16) to derive the thermochemistry for ORR and OER. The RHE model developed by Nørskov and co-workers^{35,58,60} was used to obtain the Gibbs reaction free energy of these electrochemical elementary steps. In this model, we set up RHE as the reference electrode, which allows us to replace chemical potential (μ) of the proton–electron pair with that of half a hydrogen molecule: $\mu_{\text{H}^+} + \mu_{\text{e}^-} = 1/2\mu_{\text{H}_2}$, at conditions with $U = 0$ V and $P_{\text{H}_2} = 1$ bar.

The chemical potential of each adsorbate is defined as:

$$\mu = E + E_{\text{ZPE}} - T \times S \quad (18)$$

where the E is the total energy obtained from DFT calculations, E_{ZPE} is zero-point energy and S is the entropy at 298 K. In order to obtain the reaction free energy of each elementary step of ORR, OER and HER, we calculated the adsorption free energy of O^* , OH^* , OOH^* and H^* . Because it is difficult to obtain the exact free energy of OOH , O , OH and H radicals in the electrolyte solution, the adsorption free energy ΔG_{OOH^*} , ΔG_{O^*} , ΔG_{OH^*} and ΔG_{H^*} are relative to the free energy of stoichiometrically appropriate amounts of H_2O (g) and H_2 (g), defined as follows:

$$\begin{aligned} \Delta G_{\text{O}^*} &= \Delta G(\text{H}_2\text{O}(\text{g}) + * \rightarrow \text{O}^* + \text{H}_2(\text{g})) \\ &= \mu_{\text{O}^*} + \mu_{\text{H}_2} - \mu_{\text{H}_2\text{O}} - \mu_* \\ &= (E_{\text{O}^*} + E_{\text{H}_2} - E_{\text{H}_2\text{O}} - E_*) \\ &\quad + (E_{\text{ZPE}(\text{O}^*)} + E_{\text{ZPE}(\text{H}_2)} - E_{\text{ZPE}(\text{H}_2\text{O})} - E_{\text{ZPE}(*)}) \\ &\quad - T \times (S_{\text{O}^*} + S_{\text{H}_2} - S_{\text{H}_2\text{O}} - S_*) \end{aligned} \quad (19)$$

$$\begin{aligned} \Delta G_{\text{OH}^*} &= \Delta G(\text{H}_2\text{O}(\text{g}) + * \rightarrow \text{OH}^* + 1/2\text{H}_2(\text{g})) \\ &= \mu_{\text{OH}^*} + 0.5 \times \mu_{\text{H}_2} - \mu_{\text{H}_2\text{O}} - \mu_* \\ &= (E_{\text{OH}^*} + 0.5 \times E_{\text{H}_2} - E_{\text{H}_2\text{O}} - E_*) \\ &\quad + (E_{\text{ZPE}(\text{OH}^*)} + 0.5 \times E_{\text{ZPE}(\text{H}_2)} - E_{\text{ZPE}(\text{H}_2\text{O})} - E_{\text{ZPE}(*)}) \\ &\quad - T \times (S_{\text{OH}^*} + 0.5 \times S_{\text{H}_2} - S_{\text{H}_2\text{O}} - S_*) \end{aligned} \quad (20)$$

$$\begin{aligned} \Delta G_{\text{OOH}^*} &= \Delta G(2\text{H}_2\text{O}(\text{g}) + * \rightarrow \text{OOH}^* + 3/2\text{H}_2(\text{g})) \\ &= \mu_{\text{OOH}^*} + 1.5 \times \mu_{\text{H}_2} - 2 \times \mu_{\text{H}_2\text{O}} - \mu_* \\ &= (E_{\text{OOH}^*} + 1.5 \times E_{\text{H}_2} - 2 \times E_{\text{H}_2\text{O}} - E_*) \\ &\quad + (E_{\text{ZPE}(\text{OOH}^*)} + 1.5 \times E_{\text{ZPE}(\text{H}_2)} - 2 \times E_{\text{ZPE}(\text{H}_2\text{O})} \\ &\quad - E_{\text{ZPE}(*)}) \\ &\quad - T \times (S_{\text{OOH}^*} + 1.5 \times S_{\text{H}_2} - 2 \times S_{\text{H}_2\text{O}} - S_*) \end{aligned} \quad (21)$$

$$\begin{aligned} \Delta G_{\text{H}^*} &= \Delta G(\text{H}^+ + \text{e}^- + * \rightleftharpoons \text{H}^*) \\ &= \mu_{\text{H}^*} - \mu_{\text{H}^+} - \mu_{\text{e}^-} - \mu_* \\ &= \mu_{\text{H}^*} - 0.5 \times \mu_{\text{H}_2} - \mu_* \\ &= (E_{\text{H}^*} - 0.5 \times E_{\text{H}_2} - E_*) \\ &\quad + (E_{\text{ZPE}(\text{H}^*)} - 0.5 \times E_{\text{ZPE}(\text{H}_2)} - E_{\text{ZPE}(*)}) \\ &\quad - T \times (S_{\text{H}^*} - 0.5 \times S_{\text{H}_2} - S_*) \end{aligned} \quad (22)$$

The schematic configuration of adsorbates (O , OH , OOH , H) on a single TM atom supported on functional graphite materials with diverse coordination are shown in Supplementary Fig. 28. The corresponding adsorption energies, bond lengths and bond vibrational frequencies of adsorbates are summarized in Supplementary Tables 39–54. The asterisk indicates an adsorption site. Entropy values of gaseous molecules are taken from the standard tables in *Physical Chemistry*⁶¹, while the entropies of adsorbate and adsorption sites are negligible. The zero-point energy for each adsorbate and free molecules can be obtained from the vibration frequency calculation, while the zero-point energy of adsorption sites is negligible. All the E_{ZPE} and S results are summarized in Supplementary Table 1.

For each elementary step, the Gibbs reaction free energy ΔG is defined as the difference between free energies of the initial and final states and is given by the expression:

$$\Delta G = \Delta E + \Delta \text{ZPE} - T \Delta S + \Delta G_{\text{U}} + \Delta G_{\text{pH}} \quad (23)$$

where ΔE is the reaction energy of reactant and product molecules adsorbed on catalyst surface, obtained from DFT calculations; ΔZPE and ΔS are the change in zero point energies and entropy due to the reaction. The bias effect on the free energy of each initial, intermediate and final state involving an electron in the electrode is taken into account by shifting the energy of the state by $\Delta G_{\text{U}} = -neU$, where U is the electrode applied potential relative to RHE as mentioned above, e is the elementary charge transferred and n is the number of proton–electron pairs transferred. ΔG_{pH} is the correction of the H^+ free energy and depends on whether the reaction under consideration is a reduction or an oxidation. $\Delta G_{\text{pH}} = -k_{\text{B}}T \ln[\text{H}^+] = \text{pH} \times k_{\text{B}}T \ln 10$, where k_{B} is the Boltzmann constant and T is the temperature. Hence, the equilibrium potential U_0 for four-electron transfer ORR at $\text{pH} = 14$ was determined to be 0.402 V versus NHE or 1.23 V versus RHE according to the Nernst equation ($E = E^0 - 0.0591 \text{pH}$,

$U_{\text{RHE}}^0 = U_{\text{NHE}}^0 + 0.828 \text{ V} = 0.402 + 0.828 = 1.23 \text{ V}$), where the reactant and product are at the same energy level. Given that the high-spin ground state of the oxygen molecule is poorly described in DFT calculations, the free energy of the O_2 molecule was derived according to $G_{\text{O}_2}(\text{g}) = 2G_{\text{H}_2\text{O}}(\text{l}) - 2G_{\text{H}_2} + 4 \times 1.23 \text{ (eV)}$. The free energy of OH^- was derived as $G_{\text{OH}^-} = G_{\text{H}_2\text{O}}(\text{l}) - G_{\text{H}^+}$. The free energy for gas phase water is calculated at 0.035 bars because this is the equilibrium pressure in contact with liquid water at 298 K. The free energy of gas phase water at these conditions is equal to the free energy of liquid water.

The reaction free energy of equations (9)–(12) (ΔG_1 , ΔG_2 , ΔG_3 , ΔG_4) for ORR can be calculated using the following equations:

$$\begin{aligned} \Delta G_1 &= \mu_{\text{OOH}^*} + \mu_{\text{OH}^-} - \mu_{\text{H}_2\text{O}} - \mu_* - \mu_{\text{O}_2} - \mu_{\text{e}^-} \\ &= \mu_{\text{OOH}^*} + (\mu_{\text{H}_2\text{O}} - \mu_{\text{H}^+}) - \mu_{\text{H}_2\text{O}} - \mu_* \\ &\quad - (2\mu_{\text{H}_2\text{O}} - 2\mu_{\text{H}_2} + 4 \times 1.23) - \mu_{\text{e}^-} \\ &= \mu_{\text{OOH}^*} + 1.5 \times \mu_{\text{H}_2} - 2\mu_{\text{H}_2\text{O}} - \mu_* - 4.92 \\ &= \Delta G_{\text{OOH}^*} - 4.92 \end{aligned} \quad (24)$$

$$\begin{aligned} \Delta G_2 &= \mu_{\text{O}^*} + \mu_{\text{OH}^-} - \mu_{\text{OOH}^*} - \mu_{\text{e}^-} \\ &= \mu_{\text{O}^*} + (\mu_{\text{H}_2\text{O}} - \mu_{\text{H}^+}) \\ &\quad - \mu_{\text{OOH}^*} - \mu_{\text{e}^-} \\ &= \mu_{\text{O}^*} + \mu_{\text{H}_2\text{O}} - 0.5 \times \mu_{\text{H}_2} - \mu_{\text{OOH}^*} \\ &= (\mu_{\text{O}^*} + \mu_{\text{H}_2} - \mu_{\text{H}_2\text{O}} - \mu_*) \\ &\quad - (\mu_{\text{OOH}^*} + 1.5 \times \mu_{\text{H}_2} - 2 \times \mu_{\text{H}_2\text{O}} - \mu_*) \\ &= \Delta G_{\text{O}^*} - \Delta G_{\text{OOH}^*} \end{aligned} \quad (25)$$

$$\begin{aligned} \Delta G_3 &= \mu_{\text{OH}^*} + \mu_{\text{OH}^-} - \mu_{\text{O}^*} - \mu_{\text{H}_2\text{O}} - \mu_{\text{e}^-} \\ &= \mu_{\text{OH}^*} + (\mu_{\text{H}_2\text{O}} - \mu_{\text{H}^+}) - \mu_{\text{O}^*} - \mu_{\text{H}_2\text{O}} - \mu_{\text{e}^-} \\ &= \mu_{\text{OH}^*} - 0.5 \times \mu_{\text{H}_2} - \mu_{\text{O}^*} \\ &= (\mu_{\text{OH}^*} + 0.5 \times \mu_{\text{H}_2} - \mu_{\text{H}_2\text{O}} - \mu_*) \\ &\quad - (\mu_{\text{O}^*} + \mu_{\text{H}_2} - \mu_{\text{H}_2\text{O}} - \mu_*) \\ &= \Delta G_{\text{OH}^*} - \Delta G_{\text{O}^*} \end{aligned} \quad (26)$$

$$\begin{aligned} \Delta G_4 &= \mu_{\text{OH}^-} + \mu_* - \mu_{\text{OH}^*} - \mu_{\text{e}^-} \\ &= (\mu_{\text{H}_2\text{O}} - \mu_{\text{H}^+}) + \mu_* - \mu_{\text{OH}^*} - \mu_{\text{e}^-} \\ &= \mu_{\text{H}_2\text{O}} - 0.5 \times \mu_{\text{H}_2} + \mu_* - \mu_{\text{OH}^*} \\ &= -(\mu_{\text{OH}^*} + 0.5 \times \mu_{\text{H}_2} - \mu_{\text{H}_2\text{O}} - \mu_*) \\ &= -\Delta G_{\text{OH}^*} \end{aligned} \quad (27)$$

For ORR, the onset potential is calculated by

$$U_{\text{ORR}}^{\text{onset}} = -\max\{\Delta G_1, \Delta G_2, \Delta G_3, \Delta G_4\} \quad (28)$$

The reaction free energy of equations (13)–(16) (ΔG_5 , ΔG_6 , ΔG_7 , ΔG_8) for OER, which are reverse reactions of equations (9)–(12), can be calculated using the following equations:

$$\Delta G_5 = \Delta G_{\text{OH}^*} \quad (29)$$

$$\Delta G_6 = \Delta G_{\text{O}^*} - \Delta G_{\text{OH}^*} \quad (30)$$

$$\Delta G_7 = \Delta G_{\text{OOH}^*} - \Delta G_{\text{O}^*} \quad (31)$$

$$\Delta G_8 = 4.92 - \Delta G_{\text{OOH}^*} \quad (32)$$

For OER, the onset potential is calculated by

$$U_{\text{OER}}^{\text{onset}} = -\min\{\Delta G_5, \Delta G_6, \Delta G_7, \Delta G_8\} \quad (33)$$

The HER performances were evaluated by computing the reaction free energy (ΔG_{H^*}) for hydrogen adsorption based on the computational hydrogen electrode model proposed previously³⁷ at 0 V versus RHE, that is, the equilibrium potential of the HER:

$$\Delta G_{\text{H}^*} = \Delta E_{\text{H}^*} + \Delta E_{\text{ZPE}} - T \Delta S_{\text{H}} \quad (34)$$

ΔE_{H^+} is the hydrogen adsorption energy based on DFT calculation. ΔE_{ZPE} is the zero-point energy difference between the adsorbed state and the gas-phase state of hydrogen obtained from vibrational frequency calculation. ΔS_{H} is the entropy difference due to hydrogen adsorption. Here we have approximated the entropy changes of hydrogen adsorption as $\Delta S_{\text{H}} \approx 1/2(S_{\text{H}_2})$, where S_{H_2} is the entropy of gas phase H_2 at standard conditions (300 K, 1 bar). The theoretical overpotential η for HER, which is determined by ΔG_{H^+} :

$$\eta = -|\Delta G_{\text{H}^+}|/e \quad (35)$$

The definition of the band centre of anti-bonding state ($E_{\text{anti-bond}}$). For the calculation of the band centre of the anti-bonding state projected on the sum of the d orbital of single-TM-atom and p orbital of the O atom belonging to OH^* , the following expression is used:

$$E_{\text{anti-bond}} = \frac{\int_{E_{\text{F}}}^{+\infty} E \times (\rho_{\text{d}}(E) + \rho_{\text{p}}(E)) dE}{\int_{E_{\text{F}}}^{+\infty} (\rho_{\text{d}}(E) + \rho_{\text{p}}(E)) dE} \quad (36)$$

where ρ_{d} and ρ_{p} are the density of states projected onto single-TM-atom d orbital and O atom p orbital, respectively. E_{F} is the Fermi energy.

The definition of the stability of the SAC. We check for the stability of the SAC against metal atom aggregation. The descriptor we set for this purpose is the difference between the adsorption energies of the metal atom (E_{ad}) on the functional graphene and the bulk cohesive energy (E_{coh}).

$$E_{\text{coh}} = E_{\text{bulk}} - n \times E_{\text{free-atom}} \quad (37)$$

$$E_{\text{ad}} = E_{\text{graphene+atom}} - E_{\text{graphene}} - E_{\text{free-atom}} \quad (38)$$

where n is the number of atoms in the bulk. Another descriptor we introduced to examine the stability of the SAC against the tendency of metal ion being leached is the adsorption energies of the metal atom (E_{ad}) on the functional graphene. If $E_{\text{ad}} - E_{\text{coh}} < 0$ and $E_{\text{ad}} < 0$, it is expected that SAC embedded into the graphene is more favourable than either the metal aggregation or the metal being leached, a theoretical way to confirm a material's thermodynamic stability.

Data availability. The data that support the findings of this study are available from the corresponding authors upon reasonable request.

Received: 21 November 2017; Accepted: 27 March 2018;

Published online: 30 April 2018

References

- Luo, J. et al. Water photolysis at 12.3% efficiency via perovskite photovoltaics and Earth-abundant catalysts. *Science* **345**, 1593–1596 (2014).
- Chen, C. et al. Highly crystalline multimetallic nanoframes with three-dimensional electrocatalytic surfaces. *Science* **343**, 1339–1343 (2014).
- Wang, Y. J. et al. Carbon-supported Pt-based alloy electrocatalysts for the oxygen reduction reaction in polymer electrolyte membrane fuel cells: particle size, shape, and composition manipulation and their impact to activity. *Chem. Rev.* **115**, 3433–3467 (2015).
- Holewinski, A., Idrobo, J. C. & Linic, S. High-performance Ag–Co alloy catalysts for electrochemical oxygen reduction. *Nat. Chem.* **6**, 828–834 (2014).
- Bai, X. et al. Theoretical investigation on the reaction pathways for oxygen reduction reaction on silicon doped graphene as potential metal-free catalyst. *J. Electrochem. Soc.* **163**, F1496–F1502 (2016).
- Greeley, J. et al. Alloys of platinum and early transition metals as oxygen reduction electrocatalysts. *Nat. Chem.* **1**, 552–556 (2009).
- Yang, X.-F. et al. Single-atom catalysts: a new frontier in heterogeneous catalysis. *Acc. Chem. Res.* **46**, 1740–1748 (2013).
- Qiao, B. et al. Single-atom catalysis of CO oxidation using Pt₁/FeO_x. *Nat. Chem.* **3**, 634–641 (2011).
- Wu, G., More, K. L., Johnston, C. M. & Zelenay, P. High-performance electrocatalysts for oxygen reduction derived from polyaniline, iron, and cobalt. *Science* **332**, 443–447 (2011).
- Lefevre, M., Proietti, E., Jaouen, F. & Dodelet, J. P. Iron-based catalysts with improved oxygen reduction activity in polymer electrolyte fuel cells. *Science* **324**, 71–74 (2009).
- Fei, H. et al. Atomic cobalt on nitrogen-doped graphene for hydrogen generation. *Nat. Commun.* **6**, 8668 (2015).
- Fan, L. et al. Atomically isolated nickel species anchored on graphitized carbon for efficient hydrogen evolution electrocatalysis. *Nat. Commun.* **7**, 10667 (2016).
- Chen, Y. et al. Isolated single iron atoms anchored on N-doped porous carbon as an efficient electrocatalyst for the oxygen reduction reaction. *Angew. Chem. Int. Ed.* **56**, 6937–6941 (2017).
- Zhang, X. et al. Catalytically active single-atom niobium in graphitic layers. *Nat. Commun.* **4**, 1924 (2013).
- Chen, W. et al. Rational design of single molybdenum atoms anchored on N-doped carbon for effective hydrogen evolution reaction. *Angew. Chem. Int. Ed.* **56**, 16086–16090 (2017).
- Chen, X., Chen, S. & Wang, J. Screening of catalytic oxygen reduction reaction activity of metal-doped graphene by density functional theory. *Appl. Surf. Sci.* **379**, 291–295 (2016).
- Li, X., Zhong, W., Peng, C., Li, J. & Jiang, J. Design of efficient catalysts with double transition metal atoms on C₂N layer. *J. Phys. Chem. Lett.* **7**, 1750–1755 (2016).
- Zagal, J. H., Griveau, S., Silva, J. F., Nyokong, T. & Bedioui, F. Metallophthalocyanine-based molecular materials as catalysts for electrochemical reactions. *Coord. Chem. Rev.* **254**, 2755–2791 (2010).
- Costentin, C. & Savéant, J.-M. Towards an intelligent design of molecular electrocatalysts. *Nat. Rev. Chem.* **1**, 0087 (2017).
- Zitolo, A. et al. Identification of catalytic sites for oxygen reduction in iron- and nitrogen-doped graphene materials. *Nat. Mater.* **14**, 937–942 (2015).
- Liu, W. et al. Single-atom dispersed Co–N–C catalyst: structure identification and performance for hydrogenative coupling of nitroarenes. *Chem. Sci.* **7**, 5758–5764 (2016).
- Kramm, U. I. et al. On an easy way to prepare metal–nitrogen doped carbon with exclusive presence of MeN_x-type sites active for the ORR. *J. Am. Chem. Soc.* **138**, 635–640 (2015).
- Sahraie, N. R. et al. Quantifying the density and utilization of active sites in non-precious metal oxygen electroreduction catalysts. *Nat. Commun.* **6**, 8618–8626 (2015).
- Greeley, J., Jaramillo, T. F., Bonde, J., Chorkendorff, I. B. & Nørskov, J. K. Computational high-throughput screening of electrocatalytic materials for hydrogen evolution. *Nat. Mater.* **5**, 909–913 (2006).
- Stamenkovic, V. R. et al. Trends in electrocatalysis on extended and nanoscale Pt–bimetallic alloy surfaces. *Nat. Mater.* **6**, 241–247 (2007).
- Jiao, Y., Zheng, Y., Jaroniec, M. & Qiao, S. Z. Origin of the electrocatalytic oxygen reduction activity of graphene-based catalysts: a roadmap to achieve the best performance. *J. Am. Chem. Soc.* **136**, 4394–4403 (2014).
- Suntivich, J., Gasteiger, H., Yabuuchi, N., Goodenough, J. B. & Shao-Horn, Y. Design principles for oxygen reduction activity on perovskite oxides in alkaline environment. *Nat. Chem.* **3**, 546–550 (2011).
- Tao, H. B. et al. Identification of surface reactivity descriptor for transition metal oxides in oxygen evolution reaction. *J. Am. Chem. Soc.* **138**, 9978–9985 (2016).
- Calle-Vallejo, F., Loffreda, D., Koper, M. T. M. & Sautet, P. Introducing structural sensitivity into adsorption-energy scaling relations by means of coordination numbers. *Nat. Chem.* **7**, 403–410 (2015).
- Chung, H. T. et al. Direct atomic-level insight into the active sites of a high-performance PGM-free ORR catalyst. *Science* **357**, 479–484 (2017).
- Liu, J. et al. High-performance oxygen reduction electrocatalysts based on cheap carbon black, nitrogen, and trace iron. *Adv. Mater.* **25**, 6879–6883 (2013).
- Liu, J. et al. High performance platinum single atom electrocatalyst for oxygen reduction reaction. *Nat. Commun.* **8**, 15938 (2017).
- Man, I. C. et al. Universality in oxygen evolution electrocatalysis on oxide surfaces. *ChemCatChem* **3**, 1159–1165 (2011).
- Koper, M. T. M. Thermodynamic theory of multi-electron transfer reactions: implications for electrocatalysis. *J. Electroanal. Chem.* **660**, 254–260 (2011).
- Rossmehl, J., Qu, Z. W., Zhu, H., Kroes, G. J. & Nørskov, J. K. Electrolysis of water on oxide surfaces. *J. Electroanal. Chem.* **607**, 83–89 (2007).
- Kaukonen, M., Krashennnikov, A. V., Kauppinen, E. & Nieminen, R. M. Doped graphene as a material for oxygen reduction reaction in hydrogen fuel cells: a computational study. *ACS Catal.* **3**, 159–165 (2013).
- Nørskov, J. K. et al. Trends in the exchange current for hydrogen evolution. *J. Electrochem. Soc.* **152**, J23–J26 (2005).
- Hong, W. T. et al. Toward the rational design of non-precious transition metal oxides for oxygen electrocatalysis. *Energy Environ. Sci.* **8**, 1404–1427 (2015).
- Bligaard, T. & Nørskov, J. K. *Chemical Bonding at Surfaces and Interfaces* 257–278 (Elsevier, Amsterdam, 2008).
- Yin, P. et al. Single cobalt atoms with precise N-coordination as superior oxygen reduction reaction catalysts. *Angew. Chem. Int. Ed.* **55**, 10800–10805 (2016).
- Wang, Z.-L. et al. C and N hybrid coordination derived Co–C–N complex as a highly efficient electrocatalyst for hydrogen evolution reaction. *J. Am. Chem. Soc.* **137**, 15070–15073 (2015).
- Zheng, Y., Jiao, Y., Jaroniec, M. & Qiao, S. Z. Advancing the electrochemistry of the hydrogen-evolution reaction through combining experiment and theory. *Angew. Chem. Int. Ed.* **54**, 52–65 (2015).

43. Jiang, S., Zhu, C. & Dong, S. Cobalt and nitrogen-cofunctionalized graphene as a durable non-precious metal catalyst with enhanced ORR activity. *J. Mater. Chem. A* **1**, 3593–3599 (2013).
44. Liu, X., Amiin, I. S., Liu, S., Cheng, K. & Mu, S. Transition metal/nitrogen dual-doped mesoporous graphene-like carbon nanosheets for the oxygen reduction and evolution reactions. *Nanoscale* **8**, 13311–13320 (2016).
45. Hou, Y. et al. An advanced nitrogen-doped graphene/cobalt-embedded porous carbon polyhedron hybrid for efficient catalysis of oxygen reduction and water splitting. *Adv. Funct. Mater.* **25**, 872–882 (2015).
46. Morozan, A., Goellner, V., Nedellec, Y., Hannauer, J. & Jaouen, F. Effect of the transition metal on metal–nitrogen–carbon catalysts for the hydrogen evolution reaction. *J. Electrochem. Soc.* **162**, H719–H726 (2015).
47. Baran, J. D., Grönbeck, H. & Hellman, A. Analysis of porphyrines as catalysts for electrochemical reduction of O₂ and oxidation of H₂O. *J. Am. Chem. Soc.* **136**, 1320–1326 (2014).
48. Cheon, J. Y. et al. Intrinsic relationship between enhanced oxygen reduction reaction activity and nanoscale work function of doped carbons. *J. Am. Chem. Soc.* **136**, 8875–8878 (2014).
49. Abel, M., Clair, S., Ourdjini, O., Mossoyan, M. & Porte, L. Single layer of polymeric Fe-phthalocyanine: an organometallic sheet on metal and thin insulating film. *J. Am. Chem. Soc.* **133**, 1203–1205 (2011).
50. Stepanow, S. et al. Spin tuning of electron-doped metal–phthalocyanine layers. *J. Am. Chem. Soc.* **136**, 5451–5459 (2014).
51. Kresse, G. & Furthmüller, J. Efficiency of ab-initio total energy calculations for metals and semiconductors using a plane-wave basis set. *Comput. Mater. Sci.* **6**, 15–50 (1996).
52. Kresse, G. & Furthmüller, J. Efficient iterative schemes for ab initio total-energy calculations using a plane-wave basis set. *Phys. Rev. B* **54**, 11169–11186 (1996).
53. Perdew, J., Burke, K. & Ernzerhof, M. Generalized gradient approximation made simple. *Phys. Rev. Lett.* **77**, 3865–3868 (1996).
54. Kresse, G. & Joubert, D. From ultrasoft pseudopotentials to the projector augmented-wave method. *Phys. Rev. B* **59**, 1758–1775 (1999).
55. Dudarev, S. L., Botton, G. A., Savrasov, S. Y., Humphreys, C. J. & Sutton, A. P. Electron-energy-loss spectra and the structural stability of nickel oxide: an LSDA + U study. *Phys. Rev. B* **57**, 1505–1509 (1998).
56. Mathew, K., Sundararaman, R., Letchworthweaver, K., Arias, T. A. & Hennig, R. G. Implicit solvation model for density-functional study of nanocrystal surfaces and reaction pathways. *J. Chem. Phys.* **140**, 084106 (2014).
57. Calle-Vallejo, F., Martínez, J. I., García-Lastra, J. M., Abad, E. & Koper, M. T. M. Oxygen reduction and evolution at single-metal active sites: Comparison between functionalized graphitic materials and protoporphyrins. *Surf. Sci.* **607**, 47–53 (2013).
58. Nørskov, J. et al. Origin of the overpotential for oxygen reduction at a fuel-cell cathode. *J. Phys. Chem. B* **108**, 17886–17892 (2004).
59. Desai, S. K. & Neurock, M. First-principles study of the role of solvent in the dissociation of water over a Pt–Ru alloy. *Phys. Rev. B* **68**, 1071–1086 (2003).
60. Rossmeisl, J., Logadottir, A. & Nørskov, J. K. Electrolysis of water on (oxidized) metal surfaces. *Chem. Phys.* **319**, 178–184 (2005).
61. De Paula, J. *Atkins' Physical Chemistry* (Oxford University Press, Oxford, 2010).

Acknowledgements

This work is supported by the National Natural Science Foundation of China (91634116, 21576008, 21625601).

Author contributions

D.J.C. and X.C.Z. conceived the original idea and designed the DFT calculations. D.J.C. and H.X. contributed to the density functional theory calculations. D.P.C. analysed the results. All authors wrote the manuscript and have reviewed, discussed and approved the results and conclusions of this article.

Competing interests

The authors declare no competing interests.

Additional information

Supplementary information is available for this paper at <https://doi.org/10.1038/s41929-018-0063-z>.

Reprints and permissions information is available at www.nature.com/reprints.

Correspondence and requests for materials should be addressed to D.C. or D.C. or X.C.Z.

Publisher's note: Springer Nature remains neutral with regard to jurisdictional claims in published maps and institutional affiliations.